Active-charging based powertrain control in series hybrid electric vehicles for efficiency improvement and battery lifetime extension

Xi Zhang [a,1], Chris Chunting Mi [b,*], Chengliang Yin [a,1]

[a] *Institute of Automotive Engineering, Shanghai Jiao Tong University, 800 Dong Chuan Road, Shanghai 200240, China*
[b] *Department of Electrical and Computer Engineering, University of Michigan-Dearborn, 4901 Evergreen Road, Dearborn, MI 48188, USA*

HIGHLIGHTS

- Presented an integrated powertrain control strategy for a series hybrid electric vehicle.
- Developed an ellipse-like optimized active-charging scenario and two sliding mode controllers.
- Use fixed-boundary-layer sliding mode control to guarantee robustness and eliminate chattering.
- Locate engine operation in a desired optimal area for efficiency enhancement.
- Extend battery life and at the same time, significantly improve vehicle system efficiency.

ARTICLE INFO

ABSTRACT

This paper presents a powertrain control strategy for a series hybrid electric vehicle (SHEV) based on the integrated design of an active charging scenario and fixed-boundary-layer sliding mode controllers (FBLSMCs). An optimized charging curve for the battery is predetermined rather than subject to engine output and vehicle power demand, which is a total inverse of normal SHEV powertrain control process. This is aimed to remove surge and high-frequency charge current, keep the battery staying in a high state-of-charge (SOC) region and avoid persistently-high charge power, which are positive factors to battery lifetime extension. Then two robust chattering-free FBLSMCs are designed to locate the engine operation in the optimal efficiency area. One is in charge of engine speed control, and the other is for engine/generator torque control. Consequently, not only fuel economy is improved but also battery life expectancy could be extended. Finally, simulation and experimental results confirm the validity and application feasibility of the proposed strategy.

1. Introduction

In a series hybrid electric vehicle (SHEV), propulsion power comes from the energy storage system (ESS) and the engine/generator set that converts the energy from fuel into electricity [1—5]. Compared to other vehicle types, operating noises from a SHEV are reduced dramatically, which provides the stealth function for certain military applications [4,5]. Meanwhile, engine optimal operation region could be located properly due to the particular powertrain configuration and the decoupling of mechanical link between the engine and the vehicle final drive.

Recently, the control of SHEV powertrain for emission reduction has been a research hotspot, recognizing the advantages of SHEVs. In Ref. [6], a genetic algorithm is implemented to optimally evaluate the parameters of the control algorithm for a SHEV, in order to maximize the efficiency of the powertrain while minimizing the losses. In another study, an optimal control strategy of the engine—generator subsystem was proposed to generate a desired amount of energy within a given period of time [7]. In Ref. [8], a simulated annealing (SA) algorithm was introduced to optimize the operational parameters of a SHEV fuel economy and emissions. Unfortunately, these SHEV powertrain control strategies fail to include consideration of the highly nonlinear parameter variations (e.g. generator stator leakage inductance, winding resistance, etc.) and sudden load disturbances during the vehicle operation. Therefore, satisfactory robustness usually cannot be guaranteed.

Sliding mode control (SMC) is very suitable for automotive applications due to its order reduction property and its low sensitivity

* Corresponding author. Tel.: +1 (313) 583 6434.
E-mail addresses: braver1980@sjtu.edu.cn (X. Zhang), mi@ieee.org (C.C. Mi), clyin1965@sjtu.edu.cn (C. Yin).
[1] Tel.: +86 13918913376.

to disturbances and plant parameter variations [9–13]. Nevertheless, it is known that the serious chattering phenomenon somehow prevents normal sliding mode control from real applications [12,13]. In this paper, the SHEV powertrain controller uses the chattering-free fixed-boundary-layer sliding mode controller (FBLSMC) such that the system trajectories will not vary unexpectedly at all. To locate the engine operation in the desired optimal efficiency region, two proposed sliding mode controllers responsible for engine speed and engine/generator torque respectively work together due to the simultaneous speed and torque magnitude constraints in such an area. As a result, the strong systematic robustness can be achieved against the nonlinear parameter variations and external disturbances.

Since battery technology is regarded as the key bottleneck for the large deployment of electric vehicles (EVs) and HEVs, more and more concerns are attracted from experts in the field of electrochemistry. Considerable manufacturers and researchers are focusing on improving the energy density, power density and safety of batteries [14–18]. Nevertheless, a new battery often performs unsatisfactorily in on-road tests in spite of their extraordinary test results in laboratories [19–21], because of significant differences between the laboratory and real operation conditions. For instance, in the laboratory, real on-road load (from inverter and electric motor to wheels) is usually replaced by a DC electronic load, so real high-frequency current ripples on the battery cannot appear. Additionally, a whole drive cycle for a real vehicle is seldom repeated for the laboratory test while artificial charging/discharging cycles are often performed. However, few concern the onboard systematic electrical solutions for battery lifetime extension under the present battery technology. Generally speaking, great difficulties exist in terms of precise battery lifetime prediction or test, because of unexpected application conditions and changeable battery parameters in a long term [22–25]. Fortunately, it is possible to analyze some stress factors which induce aging and influence the rate of aging of a battery [26,27]. Consequently, comparison between two aging processes with a few different factors (e.g. SOC, charge rate, temperature, etc.) is possible as long as other operating conditions are similar.

Some conditions in the conventional powertrain control can affect battery lifetime, such as surge current, persistent high power, low SOC and so on. To deal with these issues, a smooth battery charging curve (current versus SOC) is preferred, and the current value has to be large at low SOC so that the SOC can increase as quickly as possible. Thus, this paper presents an ellipse-like-based battery charge scenario. In other words, the curve of the charge current versus the battery SOC is close to an ellipse which is selected after careful comparison to other types of smooth curves. When the engine starts, the battery keeps charging at a high rate from the low SOC level, and its SOC increases fast. The charge current gradually drops to zero when the SOC approaches to the predetermined maximum level. In this case, the averagely-high SOC can be guaranteed while the persistently-high power can also be avoided. Most importantly, the chaotic and fast-variable current almost disappears, which is beneficial to battery lifetime extension. In the proposed powertrain control strategy, the power of the engine during its operation is pre-determined by power requirements of the battery and traction motor, which is an inverse power derivation process compared to that used in conventional SHEV powertrain control strategies.

Finally, in the simulation study, the integration of the proposed FBLSMCs and ellipse-like-based battery charge scenario is implemented by modifying the original SHEV model in the Advanced Vehicle Simulator (ADVISOR). The experimental setup embedded with the proposed powertrain controller design is realized, replacing the engine by an electric dynamometer. Simulation and experimental results confirm that the proposed SHEV powertrain control strategy is valid and efficient.

2. SHEV powertrain configuration

The configuration of the studied SHEV powertrain is shown in Fig. 1. An internal combustion engine (ICE) linked to a permanent magnet synchronous generator (PMSG) provides main power in hybrid mode. The generator and traction motor in this study are both permanent magnet synchronous which possesses high efficiency, high power factor, smooth torque and high power density [28–30]. The three-phase pulse-width-modulation (PWM) rectifier is utilized for the AC/DC transformation and for the quantitative energy flow out from the engine, which is capable of controlling the DC bus voltage over a wide range with unity-power-factor (UPF) operation and low total harmonic distortion (THD) of input currents [31]. A battery pack serves as the only power source in the pure-electric-vehicle (EV) mode and also absorbs the energy during regenerative braking process (braking or deceleration). In addition, the battery pack will be charged by the engine when its state of charge (SOC) drops to a predetermined level, as determined by the control strategy. The DC bus connecting the rectifier and battery pack provides the power requested by the permanent magnet synchronous motor (PMSM) which acts as the traction motor coupled to the front wheels via a drive shaft. The three-phase inverter, adaptive to both sides (the DC bus and PMSM), is used to allow quantitative bidirectional power flow as decided by the vehicle power demand.

3. Powertrain controller design

It is known that the vehicle operation process is highly nonlinear, which results in highly-nonlinear and uncertain engine dynamics. Meanwhile some parameters of the engine, generator and even the rectifier may vary during the engine operation due to the turbulences of external conditions such as temperature, pressure and so on. An effective and robust engine control methodology is in great need for enhancement of the overall system efficiency and stability.

Simple control models cannot handle complicated engine dynamics very well because they need accurate information of the system and lack of robustness that is essential to the control objective. The sliding mode control (SMC) is well known for its advantages in providing a systematic approach to the problem of maintaining stability and consistent performance facing modeling imprecision. In SMC, the system trajectory is maintained to stay on the sliding surface for subsequent time once it is driven onto this surface. However, the imperfect implementation of the control switching leads to chattering, which is a major drawback of SMC. The advantages of the fixed-boundary-layer sliding mode controller (FBLSMC) are that, not only chattering phenomenon is
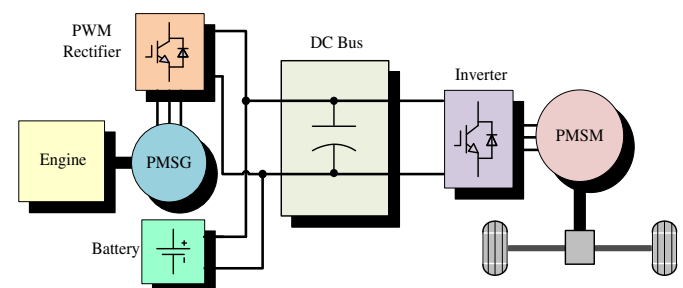

Fig. 1. The SHEV powertrain configuration studied in this paper.

removed, but also the boundary width is kept fixed so that the area where the trajectories are attracted toward the boundary is not changed, avoiding the instability of normal sliding mode controllers where system trajectories go back and forth across the sliding mode surface frequently [11]. Therefore, the FBLSMC strategy is employed in this study as an effective tool for enhancement of engine efficiency and locates engine speed and torque into the optimal area.

The proposed powertrain control strategy is based on the normal engine on/off status alternation, or thermostat control. However, different from other applications, the battery active charging for the engine-on process is pre-designed in this study. When the engine is turned on, it supplies the demanded power to the vehicle and in the meantime, the battery pack is charged by engine power and possible regenerative power following the designed optimal charging scenario. Therefore the battery SOC increases as expected. This is called the normal operation mode. Once the battery SOC reaches the predetermined maximum level, the engine controller receives a stop signal and is turned off. The operation changes to the electric vehicle (EV) mode, in which only the battery pack serves as the power source to drive the vehicle and also receives the regenerative braking power. As soon as the battery SOC drops to the given minimum level, the engine starts again preventing the battery from further depletion.

The block diagram of the proposed powertrain control system is shown in Fig. 2. The definitions of the variables in this figure are given as follows: SOC is the state of charge; V_B is the battery output voltage; I_B^r is the calculated battery charging current; P_L is the vehicle power demand; P_B^r is the required power for battery charging; $\widehat{P}_E^r$ is the engine output power with limitations; $\widehat{\omega}_E^r$ is the calculated engine speed; ω_E^* is the calculated engine speed with limitations; ω_E is the actual engine speed; $\widehat{T}_E^r$ is the calculated engine torque; T_E^* is the calculated engine torque with limitations; T_G^* is the final required generator torque; and T_G is the actual generator torque.

3.1. Engine speed control

The engine operation state function can be expressed as

$$\frac{d\omega_E}{dt} = \frac{1}{J_s} u f(\omega_E) - \frac{1}{qJ_s} T_G \tag{1}$$

where $f(\omega_E)$ stands for the maximum torque at speed ω_E, q denotes the ratio of engine speed and generator speed, which is equal to 1 in this paper, J_s is moment of inertia of the engine/generator set, and u represents the engine throttle angle (considered as the control

variable). Let $A = -1/qJ_sT_G$, $B = -1/J_s f(\omega_E)$, and the control variable could be written as

$$u = A_n^{-1}(u' - B_n) \tag{2}$$

Subscript n stands for their values under nominal parameters, and u' is considered as a new control variable. Equation (1) can be rewritten as

$$\frac{d\omega_E}{dt} = \theta_e(\omega_E) + BB_n^{-1}u' \tag{3}$$

The error function $\theta_e(\omega_E)$ is given by

$$\theta_e(\omega_E) = -\frac{1}{qJ_s}T_G + \frac{f(\omega_E)}{f(\omega_E^*)} \cdot \frac{1}{qJ_s}T_{Gn} \tag{4}$$

Let the sliding surface $s = e + \lambda \int_0^t e\,dt$, where $e = \omega_E^* - \omega_E$ and λ is a constant, and the new control variable can be obtained using the fixed boundary layer sliding mode control technology, expressed as

$$u' = -\widehat{\theta}_e(\omega_E) + \frac{d\omega_E^*}{dt} + \lambda e + (F(\omega_E) + \eta)\mathrm{msat}(\alpha, s, \phi) \tag{5}$$

where $\eta > 0$ is a predetermined constant and satisfies $s\dot{s} < -\eta|s|$.

The definition of function msat in (5) is expressed as

$$\mathrm{msat}(\alpha, s, \phi) = \begin{cases} \frac{\alpha s}{\phi} & |s| \le \phi \\ \mathrm{sgn}(s) & |s| > \phi \end{cases} \tag{6}$$

where $\alpha = \lambda\phi/F(\omega_E^*) + \eta$, and $\phi > 0$ is the width of the sliding mode layer. The maximum error function $F(\omega_E)$ and the average error function $\widehat{\theta}_e(\omega_E)$ are described by the following equations, respectively

$$F(\omega_E) = \theta_e(\omega_E)_{\max} - \theta_e(\omega_E)_{\min} \tag{7}$$

$$\widehat{\theta}_e(\omega_E) = \frac{\theta_e(\omega_E)_{\max} + \theta_e(\omega_E)_{\min}}{2} \tag{8}$$

By substituting (5) into (2), the throttle angle for the expected operation speed of the engine can be finally acquired. The engine speed control principle is depicted in Fig. 3.
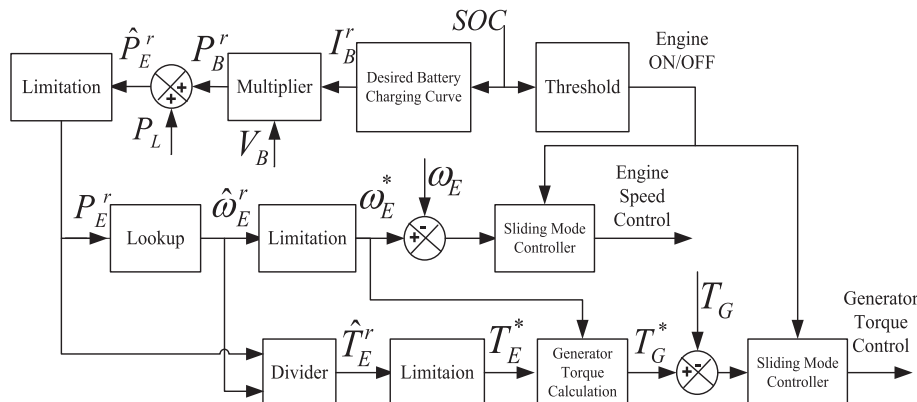
Fig. 2. Proposed powertrain control system.
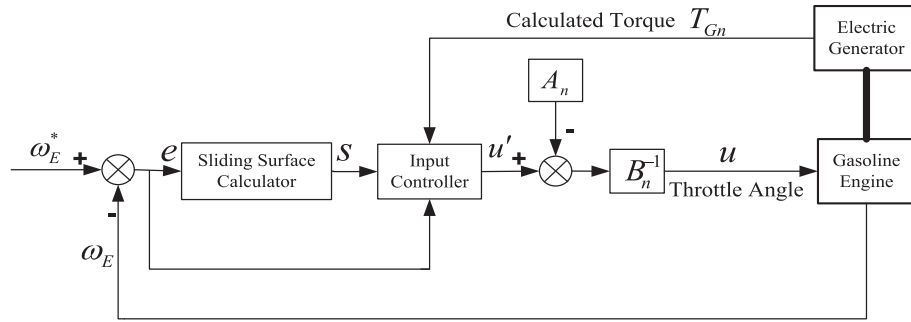
Fig. 3. Engine speed control principle.

3.2. Engine/generator torque control

The state functions of the PMSG can be described as

$$\begin{cases} T_G = K_{trq}i_q \\ \frac{di_q}{dt} = -\frac{R}{L}i_q - \omega_G i_d + \frac{\omega_G}{L}\lambda_m - \frac{u_q}{L} \\ \frac{di_d}{dt} = -\frac{R}{L}i_d + \omega_G i_q - \frac{u_d}{L} \end{cases} \quad (9)$$

where i_d and i_q are the stator direct-axis and quadrature-axis currents; L_d and L_q are the stator direct-axis and quadrature-axis inductances; λ_m is the flux of the permanent magnet; R is the stator winding resistance; $\omega_G \approx \omega_E$ is the generator speed (replaced by ω_E in the following analysis); K_{trq} is the torque constant; u_d and u_q are the stator direct-axis and quadrature-axis voltages, respectively, as control variables in the system.

Let $C = \begin{pmatrix} \theta_1(X) \\ \theta_2(X) \end{pmatrix} = \begin{pmatrix} -\frac{R}{L}i_q - \omega_E i_d + \frac{\omega_E}{L}\lambda_m \\ -\frac{R}{L}i_d + \omega_E i_q \end{pmatrix}$ and $D = \begin{pmatrix} -\frac{1}{L} & 0 \\ 0 & -\frac{1}{L} \end{pmatrix}$, and suppose

$$\begin{pmatrix} u_q \\ u_d \end{pmatrix} = D_n^{-1}\left(\begin{pmatrix} u_1 \\ u_2 \end{pmatrix} - C_n\right) \quad (10)$$

where u_1 and u_2 stand for new control variables. By substituting (10) into (9), it can be obtained that

$$\begin{pmatrix} \frac{di_q}{dt} \\ \frac{di_d}{dt} \end{pmatrix} = C - C_n + \begin{pmatrix} u_1 \\ u_2 \end{pmatrix} = \begin{pmatrix} \theta_{e1}(X) \\ \theta_{e2}(X) \end{pmatrix} + \begin{pmatrix} u_1 \\ u_2 \end{pmatrix} \quad (11)$$

where the error function may be depicted as

$$\begin{pmatrix} \theta_{e1}(X) \\ \theta_{e2}(X) \end{pmatrix} = \begin{pmatrix} \frac{R_n - R}{L}i_q + \omega_E(\lambda_m - \lambda_{mn}) \\ \frac{R_n - R}{L}i_d \end{pmatrix} \quad (12)$$

Let the sliding surface $s_i = e_i + \lambda_i \int_0^t e_i dt$, $i = 1, 2$, where $e_1 = i_q^* - i_q$, and $e_2 = i_d^* - i_d$. New controls can be obtained as

$$u_1 = -\widehat{\theta}_{e1}(X) + \frac{di_q^*}{dt} + \lambda_1 e_1 - (F_1(X) + \eta_1)\text{msat}(\alpha_1(X), s_1, \phi_1) \quad (13)$$

and

$$u_2 = -\widehat{\theta}_{e2}(X) + \frac{di_d^*}{dt} + \lambda_2 e_2 - (F_2(X) + \eta_2)\text{msat}(\alpha_2(X), s_2, \phi_2) \quad (14)$$

where $\eta_i > 0$ $(i = 1,2)$ is a predetermined constant and satisfies $s_i \dot{s}_i < -\eta_i |s_i| . (i = 1, 2)$, and $\phi_i > 0$ $(i = 1,2)$ are the widths of the two

sliding mode layers. The maximum error function $F_i(X)$ $(i = 1,2)$ and the average error function $\widehat{\theta}_{ei}(X)(i = 1, 2)$ are described by

$$F_i(X) = \theta_{ei}(X)_{max} - \theta_{ei}(X)_{min} \quad (15)$$

$$\widehat{\theta}_{ei}(X) = \frac{\theta_{ei}(X)_{max} + \theta_{ei}(X)_{min}}{2} \quad (16)$$

By substituting (13) and (14) into (10), the required stator direct-axis and quadrature-axis voltages can be finally obtained to guarantee desired generator torque. The principle for the proposed entire engine/generator torque control in real applications is shown in Fig. 4.

For analytical calculation and simulation study, a simple single-input−single-output (SISO) model [32] for the PWM rectifier as shown in Fig. 5 with the PMSG parameters (e.g. leakage inductance L, stator resistance R, etc.) is implemented through the following equations:

$$\begin{cases} L\frac{di_d}{dt} + Ri_d = e_d - (1-d)\frac{v_{dc}}{2} \\ C_f\frac{dv_{dc}}{dt} = -i_{dc} + \frac{3}{4}(1-d)i_d \\ \frac{v_{dc}}{e_d} = \frac{2}{1-D} \end{cases} \quad (17)$$

where the "equivalent" duty cycle d is defined as $d = 1 - (u_d - \omega_E L i_q / v_{dc})$; D is the steady-state equivalent duty cycle; v_{dc} is the DC bus voltage; i_{dc} is the output DC current; and e_d is the d-axis source voltage.

3.3. Optimized design of battery charging scenario

Stress factors can be considered as statistical parameters or weighted scalar variables calculated from the time series of the operating conditions, such as voltage, current, temperature and SOC, and link the operating conditions to the lifetime of batteries observed in an application [27]. Some examples of stress factors are cycling under low-state-of-charge and chaotic currents, operation at high temperature and high charging voltage or long time intervals between reaching full charge. These terms are normally used to describe empirically well-known damaging operating conditions but do not in themselves describe any irreversible changes of the battery components or materials. Stress factors only create conditions under which aging processes occur and their rate (overall or at certain locations) increases.

As mentioned earlier, it is required to design an appropriate battery charging curve to solve the problems with respect to the aforementioned stress factors e.g. chaotic and surge transient currents, persistent high power, low SOC operation, etc. Meanwhile the curve is required to satisfy the following characteristics: (1). Charging current goes down with increasing SOC, (2). The curve slope (current versus
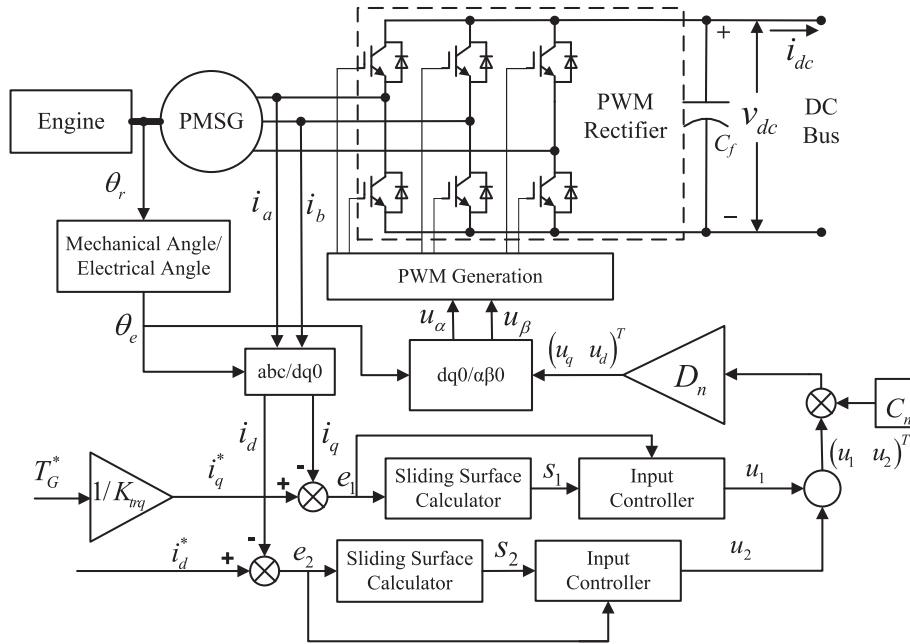
Fig. 4. Engine/generator torque control principle.

SOC) decreases from zero to nearly negative infinity to realize that SOC quickly increases to a "healthy" low threshold value in a short time, and (3). Charging current reaches nearly zero quickly when SOC is almost approaching the maximum value.

Although several options (e.g., parabola, ellipse, line, trigonometric, etc.) can be available for such charging scenarios, only ellipse curve could satisfy all the above requirements. In the meantime, the ellipse curve is easy to calculate and easy to be implemented in microprocessors. Consequently it is possible to realize in real time and in real applications. In this paper, a combination of a constant and ellipse as shown in Fig. 6 is eventually selected because the battery SOC can reach the "healthy" low threshold SOC_1 in the beginning phase (Phase I) and then approaches to the maximum value SOC_{max} in Phase II. The battery charging current I_B can be calculated as

$$
I_B = \begin{cases} I_{Bmax} & SOC_{min} < SOC < SOC_1 \\ I_{Bmax}\sqrt{1 - \left(\frac{SOC-SOC_1}{SOC_{max}-SOC_1}\right)^2} & SOC \geq SOC_1 \end{cases}
$$

(18)

where I_{Bmax} stands for the designed maximum charging current, SOC_{max} and SOC_{min} represent the predetermined maximum and minimum SOC values, respectively.

A partially linearized battery model with recovery [33] is employed to observe the actual charging current profile in the simulation study. We can make a reasonable comparison between using and not using the predetermined smooth ellipse-like current scenario. Additionally, it is important that this battery model could be used for lifetime prediction in further study. The mathematical expression of the battery model without recovery is described below

$$
\frac{dSOC(t)}{dt} = \frac{d_{2,v}}{SOC_{max}}\left(P_{bat,n}^v\right)^2 - \left[\ln\left(-SOC(t) + d_{1,v}\right) + 2d_{2,v}P_{bat,n}^v + d_{3,v}\right]\frac{P_{bat}(t)}{SOC_{max}}
$$

(19)

where $P_{bat}(t)$ is the battery power flow (positive for discharging and negative for charging); $P_{bat,n}^v$ represents the mode-dependent nominal battery operating power; v is the battery mode of operation (0 for discharging and 1 for charging); coefficient $d_{k,v}$ ($k = 1, 2, 3$), is the numerical solution to the minimization given by

$$
\min_{d_k \in R}\left\|\eta_{bat}(SOC,P_{bat},v) - \left[\ln\left(-SOC(t) + d_{1,v}\right) + 2d_{2,v}P_{bat,n}^v + d_{3,v}\right]\right\|_2
$$

(20)

The generic efficiency is expressed by $\eta_{bat}(SOC,P_{bat},v)$ in (20).

Fig. 5. Three-phase PWM rectifier circuit.
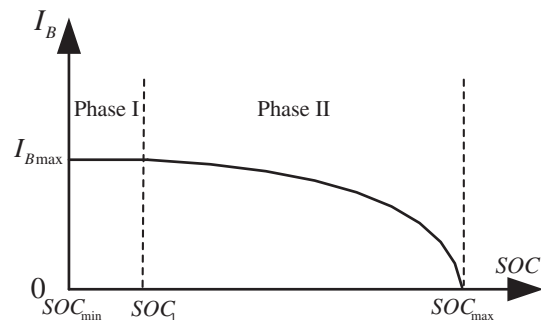
Fig. 6. Desired battery charging curve.

Table 1
Specifications of powertrain components.

Powertrain components	Specifications
SI Engine	Geo Metro 1.0L, max. power 41 kW, max. speed 5700 rpm
PMSG	Rated power 41 kW, efficiency 95%
PMSM	Rated Power 75 kW, efficiency 94%
Battery pack	81 US18650 cells in series, 20 cells in parallel, 28 A h, 3.7 V for each cell
PWM rectifier	Three IGBT/diode bridges
Inverter	Three IGBT/diode bridges

The charge recovery effect is embedded to the partially linearized battery model by augmenting an equation which is shown below

$$\frac{dSOC^r(t)}{dt} = -\frac{SOC^r(t)}{\tau} + (1+\delta)SOC(t_i), \ 0 \le P_{bat}(t) < \varepsilon \quad (21)$$

where τ is the recovery time constant; $SOC^r(t)$ represents the battery SOC during recovery; superscript r means recovery; δ denotes the recovery percentage; t_i stands for the time instance when the recovery starts; ε is a small threshold and is usually negligible compared to the discharging power loads.

For the vehicle operation, it has to be noted that the engine may not meet the calculated power requirement which is the sum of battery charging power and the peak driving power demand at the same instant. Thus constraints have to be added. As it can be seen from Fig. 2, the calculated engine power $\hat{P}_E^r$ is processed with respect to limitations, and the result P_E^r can be ensured to lie in the optimal operation region. When the calculated engine power is located in the high-efficiency region, the battery can be charged along the pre-set curve. If the calculated engine power exceeds the high-efficiency region, the driving power demand is first satisfied while the battery charging points may not lie on the pre-set curve. Whichever happens, the dynamics of the entire SHEV will not be affected at all, so the engine always operates in the optimal region, while the requirement of choosing a high-power engine could also be avoided.

4. Simulation results

This study employs Advanced Vehicle Simulator (ADVISOR) for simulation verification. The prebuilt SHEV model in ADVISOR is modified to embed the proposed control system into the powertrain. The specifications of the powertrain components are shown in Table 1. Various driving cycles are simulated but the Orange
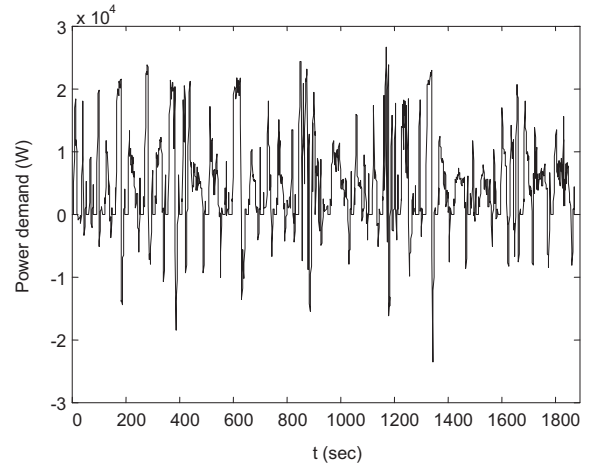

Fig. 8. Load profile of OCC.

County Cycle (OCC) is chosen as the drive cycle for discussion below. This is because the OCC comprises of considerable acceleration/deceleration processes and is capable of sufficiently validating SHEV advantages on possible improvement of system efficiency. The speed and load profiles of the OCC are shown in Figs. 7 and 8, respectively. The total vehicle mass is 1063 kg and the power demand is up to 27.4 kW. The constants in the previous analysis are set as follows for the controller development: $\lambda_1 = 3540$, $\lambda_2 = 650$, $\eta_1 = 2.03$, $\eta_2 = 2.46$, $SOC_{min} = 0.6$, $SOC_{max} = 0.8$, $SOC_1 = 0.68$.

Figs. 9 and 10 show the comparison of step responses of engine speed and generator torque between the proposed and conventional control methods. Considering the optimal operation area of the Geo Metro 1.0L SI engine, the engine/generator torque command is selected as a square wave varying between 45 Nm and 68 Nm as shown in Fig. 9. It is clear that the conventional control performs worse than the proposed control in the torque trajectory tracking since the overshoot is more than 15% and the undershoot is also bigger. The proposed strategy also shows good dynamic performance in the engine speed step response (from 220 rad s^{-1} to 365 rad s^{-1}) compared to the conventional one, which is indicated by the elimination of large overshoot and undershoot. In the meantime, real chattering phenomenon does not exist in the FBLSMCs in spite of small torque ripples related to current harmonics. Therefore, the effectiveness of the proposed FBLSMCs is verified.
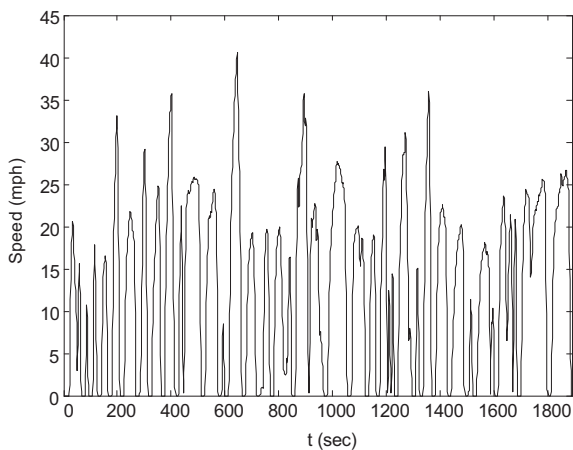
Fig. 7. Speed curve of OCC.
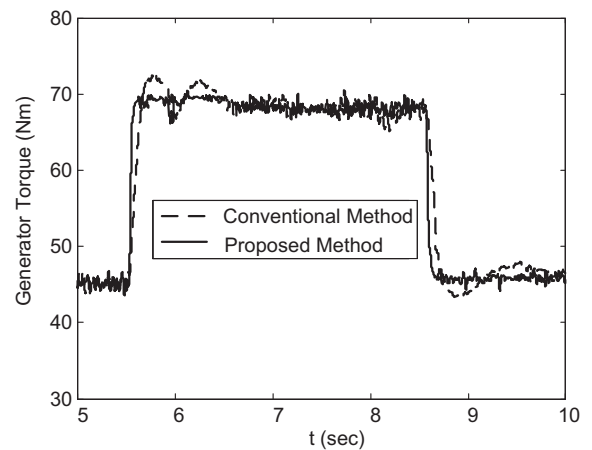
**Fig. 9.** Generator torque step response.
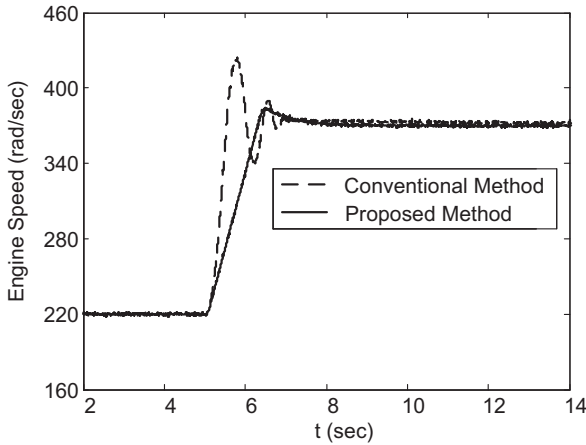
Fig. 10. Engine speed step response.

Fig. 11 shows the engine operation efficiency maps using different methods. According to statistical results, most operation points (70.4%) using the proposed strategy are located in the optimal region (within 32.1% equal-efficiency contour ranging from 210 to 380 rad s^{-1} and 45 to 68 Nm) while most operation points (64.7%) using the conventional method are beyond such an area.
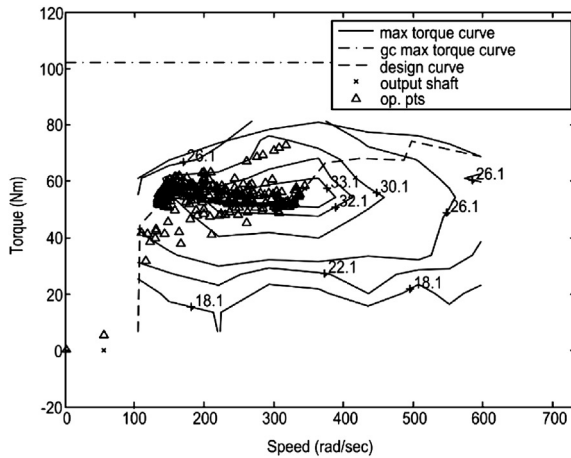

(a) The conventional method
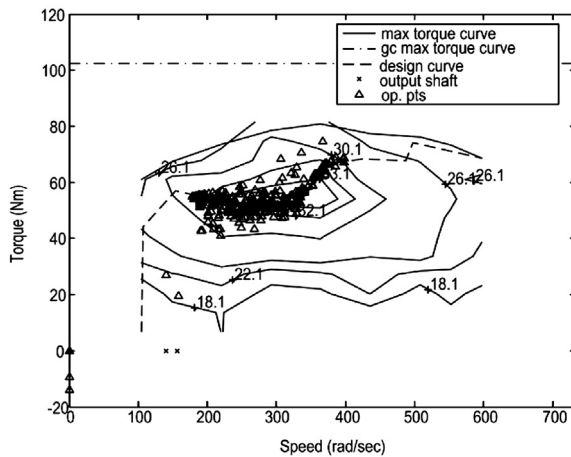
(b) The proposed method

Fig. 11. Engine operation efficiency map.
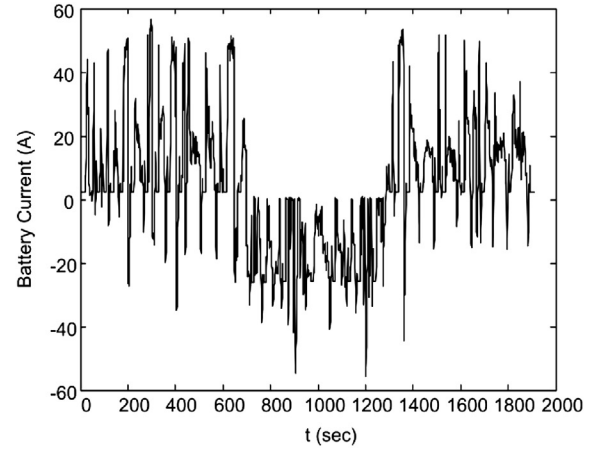
(a) The conventional method
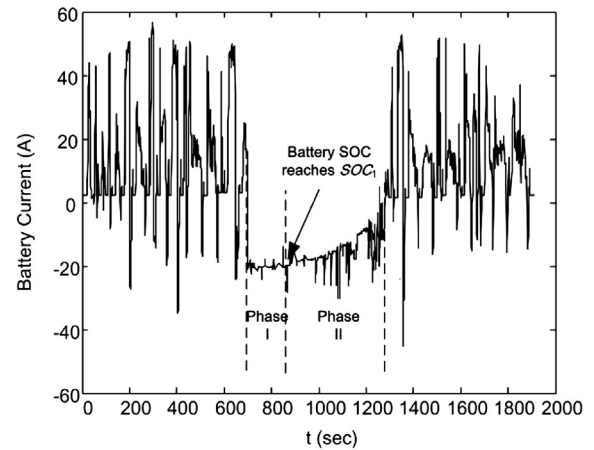
(b) The proposed method

Fig. 12. Battery current during OCC.

Consequently, the proposed strategy integrated with engine speed and generator torque coordination control could have higher engine efficiency than the conventional one.

The battery current curves in the whole OCC using the conventional and proposed methods are depicted in Fig. 12a and b, respectively. It is clear that the chaotic and surge currents using the proposed method in the normal (engine is ON) mode almost disappeared compared to those using the conventional method. This is beneficial for the battery lifetime extension. Meanwhile the battery could stay in a high SOC region longer and persistently-high charging power could be avoided, which are also positive factors to the battery health.

Table 2 gives some indexes, including MPG, emissions, and efficiency using the two methods. The MPG increases by 8.99% and the total emissions drop dramatically by 22.7%. The overall system efficiency is improved from 7.2% to 7.83% due to the engine efficiency increase by 1.9%. Thus it is concluded that the proposed method performs better in terms of fuel economy, emissions, and efficiency as well as battery lifetime expectancy.

5. Experimental results

A scaled-down experimental setup as shown in Fig. 13 was developed to validate the proposed SHEV powertrain control

**Table 2**
Performance comparison between two methods.

Index	Method	
	Conventional method	Proposed method
MPG	37.8	41.2
Emissions (g/mile)	HC: 0. 783,	HC: 0.765,
	CO: 3.234, NO_x: 0.838	CO: 2.159, NO_x: 0.827
Average engine efficiency	0.304	0.323
Overall system efficiency	0.0720	0.0783

strategy. The power demand in the experiment is 1/4 of that in the real OCC drive cycle. For the sake of simplicity of the experimental verification, a permanent magnet synchronous motor (PMSM) rated at 50 kW and 3000 rpm acts as an engine simulator to provide the required power. An identical electric machine connected to the PMSM operates under generation mode as a PMSG. The input of the PMSM is from the three-phase 380 V power grid instead of combustion of gasoline in the oil tank. A frequency converter controls the speed of the PMSM, which is similar to the situation that the throttle angle adjusts the engine speed. In the experiment, the speed and torque are both scaled down to 1/2 of the original size in the real vehicular system (so as to simulate a ¼ power demand). A three-phase PWM rectifier consisting of six IGBTs is linked with the PMSG to deliver electric power from the AC side to the DC bus where the battery is also connected. A programmable DC power supply with two isolated channels rated at 150 kW performs two roles. One is to act as a lithium ion battery simulator, and the other is to simulate the total power demand on the DC side. The DC bus voltage is set to 150 V which is nearly 1/2 of the battery voltage in the vehicular system, and the power demand is 1/4 of that in the real OCC drive cycle as mentioned above. It could be inferred that the battery current is 50% scaled down. A TI DSP2812 chip is responsible for receiving the torque/current command and meanwhile for PWM signal generation and data acquisition of the rectifier. A host computer sends the power demand command to the programmable DC system according to the power data of the OCC drive cycle. Most importantly, the host computer also calculates the optimal speed and torque/current commands based on the algorithm in Section 2 with respect to the simulated SOC data from the programmable DC system.
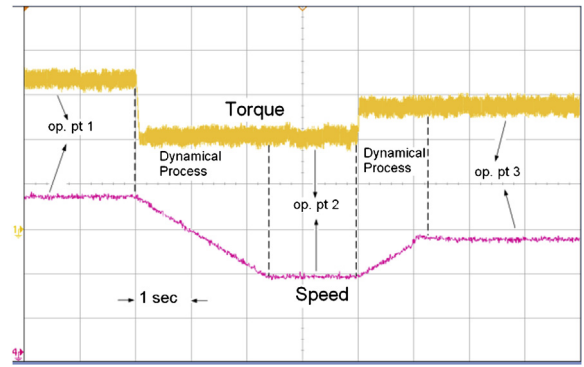
Fig. 14. Experimental results of engine operation shift.

To prove the validity of proposed powertrain controller for engine operation shift in the optimal efficiency area as depicted in Fig. 11, three optimal operation points are considered for torque and speed command generation. They are (42.2 Nm, 210 rad s^{-1}), (66.4 Nm, 403 rad s^{-1}) and (54.5 Nm, 302 rad/s^{-1}), respectively. In the experiment, the speed and torque are both scaled down to 1/2 of their original size as mentioned above. Thus, the operation points for the PMSM speed and PMSG torque commands are resized to (21.1 Nm, 105 rad s^{-1}), (33.2 Nm, 202 rad s^{-1}) and (27.3 Nm, 151 rad s^{-1}), respectively. The experimental results for the shift process are shown in Fig. 14. It can be seen that the PMSG torque responds quickly to the reference under the step command by sending the appropriate PWM signals (generated from the torque FBLSMC) to the rectifier. The response time is below 150 ms. Meanwhile, the PMSM simulating an internal combustion engine (ICE) could easily track the desired speed command taking into account the actual response period (within a few seconds) of a real engine. Consequently, the operation shift of the engine for the optimal location is available using the proposed powertrain control strategy.

The entire OCC drive cycle data is imported to the host computer and the experiment is carried out to verify the desired charging current scenario. The battery capacity is considered as 1/2 of the real capacity (due to voltage also reduces by 1/2) to reach ¼ of power demand of the vehicular system for the simulated SOC
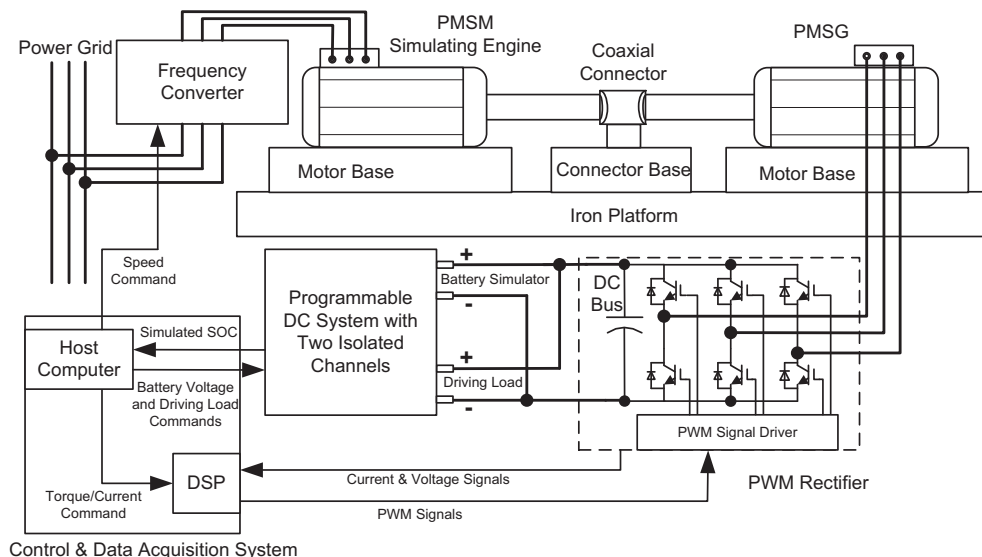
**Fig. 13.** Experimental setup block diagram.
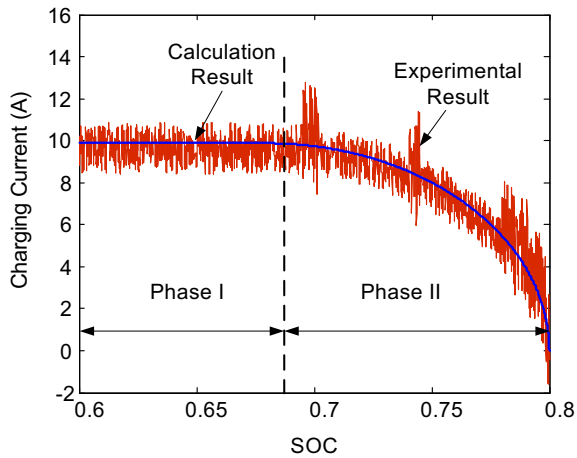
Fig. 15. Experimental results of battery charging current versus SOC during OCC driving cycle.

calculation. It has to be noted that the battery charging current may exist some small spikes larger than the expected value in the designed scenario. This is because that sudden regenerative braking power results in power increase to the battery although the engine (PMSM in experiments) reduces its output power dramatically. The experimental result of battery charging current versus SOC is shown in Fig. 15. It can be seen that the current curve indicates very typical characteristics of the two phases proposed in this paper, i.e., a constant-current phase and an ellipse-charging phase. Some increasing current spikes occur at SOC of about 0.70, 0.74 and 0.78–0.797 due to the regenerative braking power which reach 4.03 kW, 4.08 kW and 2.5 kW, respectively, in the experimental operation. However, it is acceptable that the current error is controlled between −2A and 3A at these times. On the other hand, the battery charging current error is less than ±2A in the whole process except the above time instants. Most importantly, frequent large chaotic and surge currents always varying from zero to maximum values in the whole process have disappeared. The other positive factors for battery lifetime extension also work as analyzed above. As a result, the current lifetime expectancy could be improved by use of the proposed powertrain control system.

6. Conclusion

With the proposed active-charging-based SHEV powertrain control, an optimized charging curve for the battery considering lifetime extension could be predetermined rather than subject to engine output and vehicle power demand. Meanwhile, the engine speed and engine/generator torque are controlled to reach the optimal operation area in the engine efficiency map through the design of two fixed-boundary-layer sliding mode controllers (FBLSMCs). It is meaningful that the proposed strategy is capable of not only improving engine and entire system efficiency but also extending the battery lifetime expectancy. The simulation results validated the proposed method using the Advanced Vehicle Simulator (ADVISOR) software. Experiments on the basis of an

established control system including a host computer and a DSP also demonstrate the applicability of the proposed strategy to the real system.

References

[1] V. Sezer, M. Gokasan, S. Bogosyan, IEEE Trans. Veh. Technol. 60 (8) (Oct. 2011) 3557–3570.
[2] S. Park, A.A. Malikopoulos, M. Kokkolaras, Michael, D. Jung, Int. J. Heavy Veh. Syst. 18 (3) (Jul. 2011) 272–287.
[3] C.E. Nino-Baron, A.R. Tariq, G. Zhu, E.G. Strangas, IEEE Trans. Veh. Technol. 60 (6) (Jul. 2011) 2438–2447.
[4] D. Milner, J. Goodell, W. Smith, M. Pozolo, J. Ueda, World Electr. Veh. J. 3 (1) (Jan. 2009).
[5] E. Galvagno, E. Rondinelli, M. Velardocchia, Int. J. Heavy Veh. Syst. 19 (3) (Jul. 2012) 256–280.
[6] M. Amiri, M. Esfahanian, M.R. Hairi-Yazdi, J. Power Sources 190 (2) (May 2009) 372–379.
[7] H. Yoo, S.K. Sul, Y. Park, J. Jeong, IEEE Trans. Ind. Appl. 44 (1) (Jan.–Feb. 2008) 108–114.
[8] Z. Wang, B. Huang, Y. Xu, W. Li, Optimization of series hybrid electric vehicle operational parameters by simulated annealing algorithm, in: 2007 Int. Conf. Control Autom. (ICCA), Guangzhou, China, 2007, pp. 1536–1541.
[9] H. Imine, T. Madani, Int. J. Robust Nonlinear Control 23 (1) (Jan. 2013) 67–76.
[10] H. Zhou, Z. Liu, IEEE Trans. Veh. Technol. 59 (7) (Sept. 2010) 3674–3678.
[11] F. Cupertino, D. Naso, E. Mininno, B. Turchiano, EEE Trans. Ind. Appl. 45 (5) (Sept. 2009) 1688–1696.
[12] J. Javadi-Moghaddam, A. Bagheri, Expert Syst. Appl. 37 (1) (Jan. 2010) 647–660.
[13] B. Allaoua, A. Laoufi, J. Electr. Eng. Technol. 6 (1) (Jan. 2011) 67–75.
[14] A. Cooper, J. Furakawa, L. Lam, M. Kellaway, J. Power Sources 188 (2) (Mar. 2009) 642–649.
[15] P. Aguiar, D.J.L. Brett, N.P. Brandon, J. Power Sources 171 (1) (Sept. 2007) 186–197.
[16] X. Wang, B. Wu, K. Yang, X. Yang, C. Wu, F. Wang, F. Wu, S. Chen, G. Li, J. New Mater. Electrochem. Syst. 12 (4) (Oct. 2009) 213–217.
[17] J. Bains, L. Croguennec, J. Bréger, F. Castaing, S. Levasseur, C. Delmas, P. Biensan, J. Power Sources 196 (20) (Oct. 2011) 8625–8631.
[18] M.L. Soria, F. Trinidad, J.M. Lacadena, A. Sánchez, J. Valenciano, J. Power Sources 168 (1) (May 2007) 12–21. SPEC. ISS.
[19] S.B. Peterson, J. Apt, J.F. Whitacre, J. Power Sources 195 (8) (Apr. 2010) 2385–2392.
[20] U.K. Madawala, D.J. Thrimawithana, IEEE Trans. Ind. Electron. 58 (10) (Oct. 2011) 4789–4796.
[21] Y. Hu, S. Yurkovich, Y. Guezennec, B.J. Yurkovich, J. Power Sources 196 (1) (Jan. 2011) 449–457.
[22] M. Ecker, J.B. Gerschler, J. Vogel, S. Käbitz, F. Hust, P. Dechent, D.U. Sauer, J. Power Sources 215 (Oct. 2012) 248–257.
[23] D.P. Jenkins, J. Fletcher, D. Kane, IET Renew. Power Gener. 2 (3) (Jul. 2008) 191–200.
[24] T. Weigert, Q. Tian, K. Lian, J. Power Sources 196 (8) (Apr. 2011) 4061–4066.
[25] D. Kawasaki, H. Ishikawa, S. Sudo, K. Utsugi, NEC Tech. J. 7 (1) (Mar. 2012) 60–63.
[26] J. Schiffer, D.U. Sauer, H. Bindner, T. Cronin, P. Lundsager, R. Kaiser, J. Power Sources 168 (1) (May 2007) 66–78. SPEC. ISS.
[27] R. Kaiser, J. Power Sources 168 (1) (May 25, 2007) 58–65. SPEC. ISS.
[28] Y. Li, D. Gerling, J. Ma, J. Liu, Q. Yu, World Electr. Veh. J. 4 (1) (Jan. 2011) 648–654.
[29] J. Lee, K. Nam, S. Choi, S. Kwon, IEEE Trans. Power Electron. 24 (4) (Apr. 2009) 1071–1082.
[30] R. Guclu, K. Gulez, Math. Comput. Model. 47 (11–12) (Jun. 2008) 1356–1371.
[31] A. Bouafia, F. Krim, J.P. Gaubert, IEEE Trans. Ind. Appl. 56 (6) (Jun. 2009) 1984–1992.
[32] B. Yin, R. Oruganti, S.K. Panda, A.K.S. Bhat, IEEE Trans. Power Electron. 24 (3) (Mar. 2009) 620–631.
[33] V. Agarwal, K. Uthaichana, R.A. Decarlo, L.H. Tsoukalas, IEEE Trans. Energy Convers. 25 (3) (Sept. 2010) 821–835.